Modeling of Terahertz Heating Effects in Realistic Tissues

Sashikumaar Ganesan and Phaneendra K. Yalavarthy

***Abstract*—The terahertz propagation in real tissues causes heating as with any other electromagnetic radiation propagation. A finite element model that provides numerical solutions to the heat conduction equation coupled with realistic models of tissues is employed in this work to compute the temperature raise due to terahertz propagation. The results indicate that the temperature raise is dependent on the tissue type and is highly localized. The developed finite element model was validated through obtaining solutions for the steady-state case and showing that they were in good agreement with the analytical solutions. These type of models can also enable computation of specific absorption rates, which are very critical in planning/setting up experiments involving biological tissues.**

***Index Terms*—Far infrared, Terahertz Heating, Breast and Brain, Finite Element Modeling.**

I. Introduction

TERAHERTZ (THz) technology advances in biomedical arena [1] has resulted in promising applications, including breast [2], [3], skin [4], and hard tissue imaging/spectroscopy [5]. The recent advances in THz time domain spectroscopy (TDS) studies have made THz as one of strong contender for sensing and detection in defense applications [6], [7].

The THz uses far infrared spectrum of wavelengths and known to be a non-ionizing type of radiation making it well suited for biomedical applications [1]-[5]. These THz systems are based on photoconductive switches that produce an average power around 1 μW. But the modern THz systems use more powerful quantum cascade lasers or free electron lasers, which have the capabilities to produce the average power ranging from 1 mW to 20 W [8]-[11]. These systems could cause permanent damage to the biological tissues under investigation when the exposure time is sufficiently large, compelling a detailed investigation of the THz exposure for better understanding of its effects. As with any other electromagnetic radiation interaction with tissue, the temperature distribution as a consequence of THz absorption is determined by the heat transfer mechanisms of conduction, convection, and radiation [12]. Determining such temperature elevation due to THz absorption is critical, as dielectric properties of tissues vary with temperature [12] and the detected THz signal is known to be sensitive to dielectric properties [13].

The heating effects of THz radiation in biological tissue have been investigated in the recent past [14], [15], with skin and water as case studies. These studies are inherently very useful in determining the heating effects and give first hand information about these, the models including the solutions were too simplistic to understand the transient behavior of heating effects. The work of Kristensen et. al [15] have assumed a static (steady-state) model and derived the analytical solution for the Kirchoff's heat equation for the case of water. This study has motivated the current work, where the transient behavior in realistic models consisting of different tissue types are considered here. The input parameters for these tissue types were identified from the literature. The realistic models here were both brain and breast models (Figs. 1 and 2), as these are irregular geometries, a numerical scheme based on Finite-Element-Method (FEM) was used to perform this study. This work also includes the investigation of showing that the FEM-based numerical scheme is in good agreement with the analytical solution proposed in Ref. [15]. As in the case of Ref. [15], the discussion here is limited to continuous-wave THz propagation with frequency of 1 THz and the specification of source is in terms of beam diameter and power (rather than power density).

Even though the realistic tissues that were considered here are only breast and brain models, the numerical scheme can be easily extended to other tissue model as well. The choice of FEM as the numerical method compared to others, such as finite difference, is due to flexibility offered by FEM in terms of solving the partial differential equation (in here, heat conduction equation) in irregular geometries.

As a part of this work, the finite element (FE) mesh size and the THz beam spot diameter effect on the temperature raise is studied along with transient behavior showing the dependency of temperature raise in the realistic models as a function of exposure time.

II. Methods

A. Finite Element Modeling

Let the computational domain $\Omega \subset \mathbb{R}^3$, which may have several regions, be open and bounded. The heat transfer in Ω which is exposed to a THz radiation in the time interval $(0, I)$ is described by the heat conduction equation [12]

$$\begin{aligned} \rho c_p \frac{\partial T}{\partial t} - \nabla \cdot (k \nabla T) &= f \quad \text{in} \quad \Omega \times (0, I) \\ T &= T_0 \quad \text{on} \quad \Gamma \\ k \nabla T \cdot n &= 0 \quad \text{on} \quad \partial\Omega \setminus \Gamma \\ T(\cdot, 0) &= T_0 \quad \text{in} \quad \Omega. \end{aligned} \tag{1}$$

Here, $\rho(x, y, z)$ denotes the density (kg m^{-3}), $c_p(x, y, z)$ the specific heat (J K^{-1} kg^{-1}), $k(x, y, z)$ the thermal conductivity

Manuscript received April 1, 2012; revised June 26, 2012 and July 6, 2012.

S. Ganesan and P. K. Yalavarthy are with the Supercomputer Education and Research Centre, Indian Institute of Science, Bangalore, India - 560012. (e-mail: sashi@serc.iisc.in; phani@serc.iisc.in)

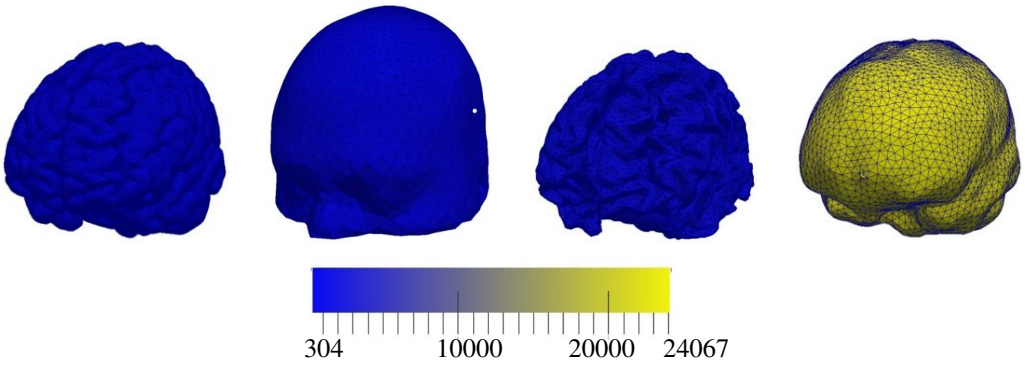

Fig. 1. Iso-surfaces of different tissue types in the brain model, namely (left to right) gray matter, scalp/skull, white matter, and CSF layer. The colorbar depicts the absorption coefficient (α in m^{-1}) for brain tissue types. The THz source location is specified as a white spot on the skull surface.

(W m^{-1} K^{-1}), $T(x,y,z,t)$ the temperature (K), t the time (s), I the given end time (s), Γ the Dirichlet part of the boundary $\partial\Omega$, and T_0 the body temperature. Further f is the dissipated power density, and in the z-direction it can be defined as follows. Let (x_p, y_p, z_p) on the surface $\partial\Omega$ be the center of the THz beam. We first transform the domain in z-coordinate using the transformation $\hat{z} = z - z_p$, so that the center of the THz beam becomes $(x_p, y_p, 0)$. Now, we define the source term in z-direction by

$$f = \begin{cases} \dfrac{\alpha P}{\pi a^2} \exp(-\alpha|\hat{z}|) & \text{for} \quad 0 \le r \le a \\ 0 & \text{else,} \end{cases}$$

where α the absorption coefficient (m^{-1}), P the transmitted power (W), a the THz beam radius (m), and $r = \sqrt{(x-x_p)^2 + (y-y_p)^2}$. Note that the source in other coordinate directions can also be defined in a similar way.

In our model, we assume that the parameters ρ, c_p and k are constants in each region of the domain but may have jumps across the regions. We first transform the temperature using the transformation $\hat{T} = T - T_0$ (indicating that our interest is only in computing the raise in temperature), and then scale the domain Ω with the characteristic length L to get

$$\begin{aligned} \frac{\partial \hat{T}}{\partial t} - \frac{1}{\rho c_p L^2} \nabla \cdot (k \nabla \hat{T}) &= \hat{f} \quad \text{in} \quad \hat{\Omega} \times (0, I) \\ \hat{T} &= 0 \quad \text{on} \quad \hat{\Gamma} \\ k \nabla \hat{T} \cdot n &= 0 \quad \text{on} \quad \partial\hat{\Omega} \setminus \hat{\Gamma} \\ \hat{T}(\cdot, 0) &= 0 \quad \text{in} \quad \hat{\Omega}, \end{aligned} \tag{2}$$

where

$$\hat{f} = \begin{cases} \dfrac{1}{\rho c_p} \dfrac{\alpha P}{\pi a^2} \exp(-\alpha|\hat{z}|L) & \text{for} \quad 0 \le r \le a \\ 0 & \text{else,} \end{cases} \tag{3}$$

Next, to solve the heat conduction equation by FEM [16] we first derive the variational form. In order to impose the homogenous Dirichlet boundary condition in the ansatz and test spaces we define $V = \{v \in H^1(\Omega) : v = 0 \text{ on } \Gamma\}$, where $H^1(\Omega)$ is the usual Hilbert space. Now, we multiply the heat conduction equation (Eq. 2) by a test function $v \in V$ and integrate it over Ω. After applying integration by parts to the second term in Eq. 2 and incorporating boundary conditions, the variational form becomes:

For given $f \in L^2((0,I] \times \Omega)$, find $\hat{T} \in L^2(0, I; V)$ with $T' \in L^2(0, I; V^{-1})$ such that

$$\left(\frac{\partial \hat{T}}{\partial t}, v\right) + \left(\frac{k}{\rho c_p L^2} \nabla \hat{T}, \nabla v\right) = \left(\hat{f}, v\right) \quad \forall\, v \in V. \tag{4}$$

Here, $(\cdot,\cdot)$ denotes the inner product in the Lebesque space $L^2(\Omega)$ and V^{-1} is the dual space of V.

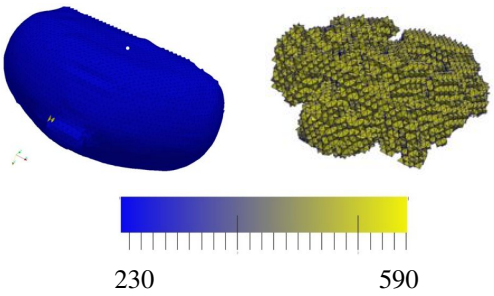

Fig. 2. Iso-surfaces of the tissue types in the breast model used, namely (from left to right) fatty/adipose and fibro-glandular tissue. The colorbar depicts the absorption coefficient (α in m^{-1}) for breast tissue types. The THz source location is specified as a white spot on the fatty tissue surface.

TABLE I
INPUT PARAMETERS FOR VARIOUS TISSUE TYPES IN THE REALISTIC MODELS USED IN THIS WORK. THE FIRST FOUR ROWS OF THE TABLE CORRESPOND TO THE BRAIN MODEL USED AND REST FOR BREAST MODEL.

	ρ	c_p	k	α
water/CSF	997	3710	0.6064	24067
scalp and skull	1600	2000	0.3	327
gray matter	1030	3854	0.528	304
white matter	1030	3854	0.528	1000
fat	1100	4483	0.204	230
fibrous	1040	3500	0.518	590

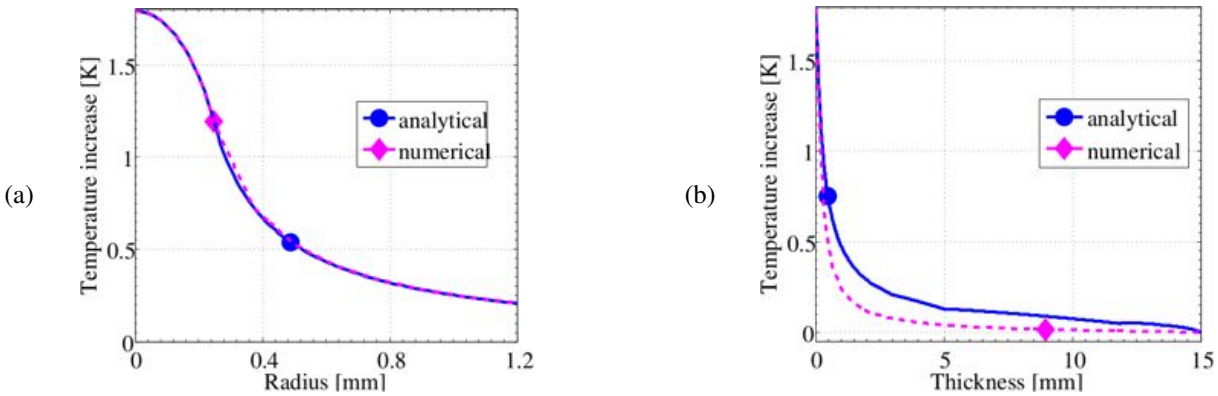

Fig. 3. Comparison of steady-state solution using analytical model [15] and the FEM based model for cylindrical domain. The variation in (a) radial and (b) axial directions are plotted with temperature raise as the parameter.

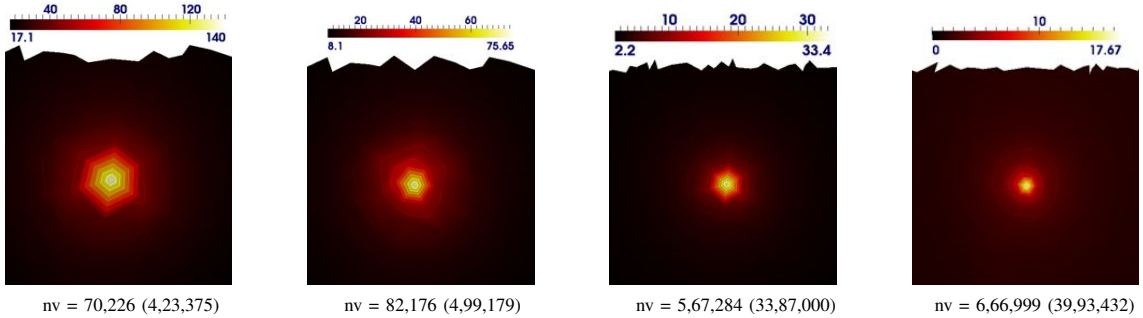

Fig. 4. Mesh size dependent behavior of temperature raise in the region of interest (60 mm X 60 mm centered around source, shown in Fig. 1) in the brain model using the steady-state equation. The number of vertices (nv) of the FE mesh in each case are given in the bottom of each figure, the corresponding tetrahedral elements are indicated in parenthesis. The input parameters for the model are given in Table-I with THz beam radius $a = 0.25$ mm with the power $P = 1$ mW.

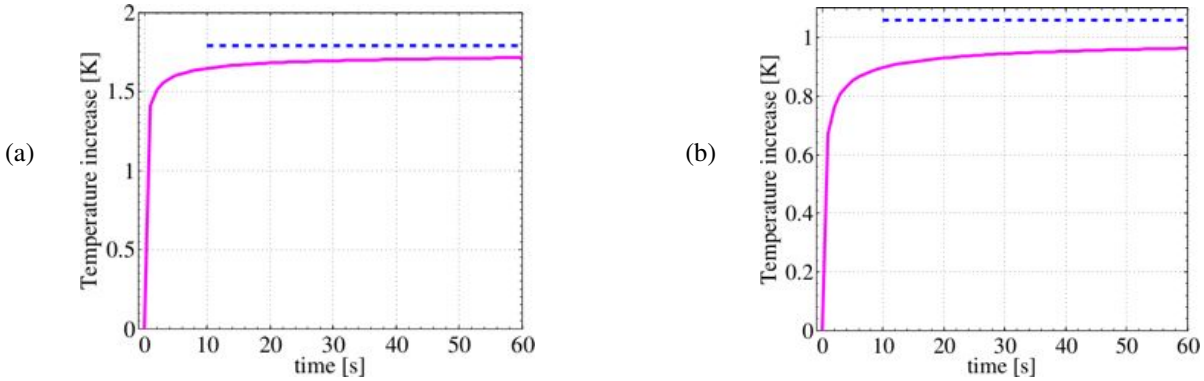

Fig. 5. Time-dependent solutions for cylindrical domain using finite element method at (a). source location and (b). 0.28 mm along the radial direction for first one minute. The dashed line indicates the steady-state solution. Note that THz beam radius is $a = 0.25$ mm with the power $P = 1$ mW.

Let $0 = t^0 < t^1 <, \ldots, t^N = I$ be the decomposition of the time interval $[0, I]$, and $\delta t = t^{n+1} - t^n$ be an uniform time-step. Now, using the first-order, implicit backward Euler method the semi-discrete (in time) form of Eq. 4 in the time interval (t^n, t^{n+1}) reads:
For given T^n, find $T^{n+1} \in V$ such that

$$\left(\hat{T}^{n+1}, v\right) + \delta t \left(\frac{k}{\rho c_p L^2} \nabla \hat{T}^{n+1}, \nabla v\right) = \delta t \left(\hat{f}^{n+1}, v\right) + \left(\hat{T}^n, v\right) \quad \forall\, v \in V.$$

We triangulate the domain Ω into linear tetrahedra cells, and use the piecewise linear finite element on each tetrahedron cell. Finally, we obtain the system of linear equations in the time interval (t^n, t^{n+1}) as [16]

$$(M + \delta t A)\, T^{n+1} = \delta t F^{n+1} + M T^n. \tag{5}$$

Here, M and A are the mass and the stiffness matrices, respectively. Further, F is the load vector. The matrices and the load vector are assembled in parallel. In our parallel algorithm we first decompose the collection of tetrahedra cells into N_P number of sub-collection of cells using the package METIS [17], where N_P is the number of processors used in simulation. Then, we assemble the local matrices and load

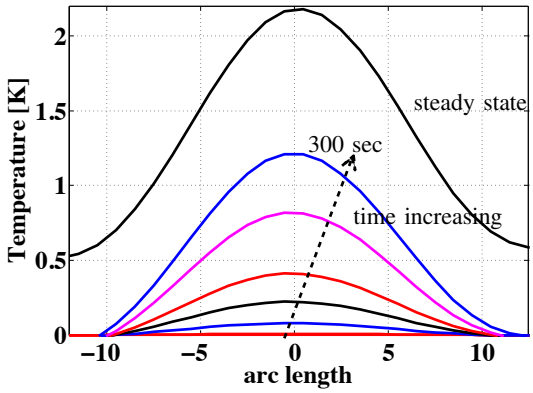

Fig. 6. An one-dimensional plot showing the time-dependent behavior of temperature raise around source (arc length = 0) in the brain model. The time points that were shown here correspond to 0.5, 1, 10, 30, 60, 150, and 300 sec along with steady-state solution. The input parameters for the model are given in Table-I with THz beam radius $a = 2$ mm with the power $P = 1$ mW.

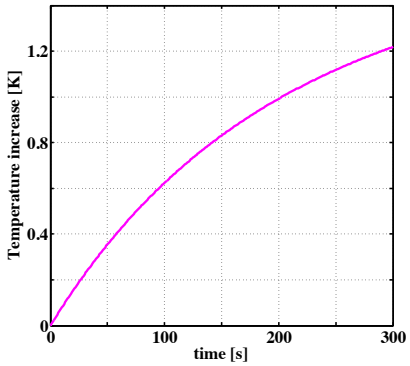

Fig. 7. The transient behavior of temperature raise at the source location corresponding to Fig. 6.

vector on each processor. Finally, we solve the algebraic system using the parallel solver MUMPS [18]. Note that the matrices and the load vector are independent of time. Thus, it is enough to assemble it only once at the start of the simulation. All computations were carried out on a Linux server with 2.4 GHz 32-core AMD processor having 128 GB RAM.

B. Computational Models

We consider three different computational domains in this study. The first model is a cylindrical domain, which mimics the 3D-axisymmetric geometry used in Ref. [15], assumed to be filled with water. The radius and the height of the cylinder are 50 mm and 15 mm, respectively. Using the TetGen mesh generator [19], we triangulate the cylinder and obtain 23666 vertices and 111573 tetrahedral cells. This model is used to validate our finite element scheme. Next, we consider the Collins adult brain atlas [20], [21] FEM mesh Version 1 for the THz radiation study. The original brain atlas mesh consists of 70,226 vertices and 4,23,375 tetrahedral cells. Further, the brain atlas mesh contains scalp/skull, CSF, gray-matter and white-matter regions, see Fig. 1. The properties of the same were obtained from literature [12], [23], [24] that were used in the model are listed in Table-I. Next, we consider a breast mesh generated using MR-images [22], consisting of 31,910 vertices and 1,73,101 tetrahedral cells. The fat and the fibrous regions of the breast mesh are shown in Fig. 2. Similar to the brain tissue, the breast tissue model properties are given in Table-I.

III. Results

A. Comparison of analytical and Steady-State FEM solution

To validate the finite element scheme, we first solve the Kirchoff's (steady-state) heat equation, and compare the numerical solution with the analytical solution provided in Ref. [15]. A THz beam of radius $a = 0.25$ mm with the power $P = 1$ mW is transmitted at the origin $(0, 0, 0)$. The numerically obtained change in the temperature at $z = 0$ plane as a function of radial distance is plotted in Fig. 3 (a). The finite element solution is in good agreement with the analytical solution, see Fig. 3 (a). Next, the temperature change from the origin $(0, 0)$ with varying height (thickness) z is plotted in Fig. 3 (b). Here, the numerical solution coincides with analytical solution up to the thickness, say $z = 1$ mm, where the mesh is very fine in this region. In comparison with the analytical solution the numerical solution varies slightly when the thickness increases. Since the mesh becomes very coarser when the thickness increases (the effect of mesh size is studied separately), this could be the reason for the variation in numerical solution. Nevertheless, we obtain the similar behavior in the numerical solution as compared to analytical solution.

B. Effect of mesh size on the steady-state FEM solution

The FE mesh size (number of vertices/elements) is known to impact accuracy of the solution especially in the area of illumination [25]. The mesh size indicates the spatial discretization of the tissue under investigation and is important to consider for knowing the accuracy of the computed solution. For this study, we have considered steady-state case of the heat-conduction equation and used it on the brain model with varying nodal density. Due to the diffraction limit, it is hard to focus the 1 THz beam down to spot radius of smaller than 0.25 mm [14], which is considered in here as the worst case with the power $P = 1$ mW. Figure 4 shows the obtained solutions in the region of interest (ROI) with decreasing the mesh size (number of vertices are given at the bottom of each distribution), which clearly shows that the model having smaller mesh size gave more stable solution. Note that increase in the number of vertices beyond 6,66,999 did not result in significant change in the computed temperature. These meshes with varying spatial discretization were obtained as follows: the mesh with 70,226 vertices is the original Collins adult brain atlas, the mesh with with 82,176 vertices is obtained by refining the surface mesh near the ROI and adapted the tetrahedron cells accordingly, where as the meshes with 5,67,284 and 6,66,999 vertices are obtained by uniform refinement of the original mesh and the adaptive mesh, respectively. The discrepancy in the computed temperatures is primarily due to the coarseness of the mesh to model the source (Eq. 3) accurately, as the distance between

the nodes is less or equal to spot diameter (which is the case for the last column of Fig. 4), the solutions showed no significant numerical errors. Also, this study when repeated for breast mesh the variation in the computed temperatures were not significantly varying indicating that the original breast mesh has sufficient spatial discretization. Note that in cases where the spot radius is higher than 1 mm, the original mesh (first column) itself provided enough robustness to the numerical solution as the nodal distance was atleast equal to the spot diameter.

C. Time-dependent FEM Solutions

Cylindrical Domain: Next, we solve the time-dependent heat conduction equation (Eq. 1) in the cylindrical domain with the same input parameters as in the above steady-state case. We use an uniform time step $\triangle t = 0.01$ sec in all computations. The time dependent behavior of the solution for this case is depicted in Fig. 5 using two test points. The dashed horizontal line in Fig. 5 shows the steady-state solution for comparison. As the time progresses the transient behavior of the temperature raise slowly decreases and reaches the steady-state solution.

D. Brain Tissue

For the case of realistic tissues, the source radius was different compared to the cylindrical domain case. In the cylindrical domain case, an uniform THz beam profile is used to reproduce the numerical experimental conditions performed in Ref. [15]. In this case, a beam radius of 2 mm is used for THz source with a power of 1 mW along with original brain atlas mesh. The transient behavior of the solutions when the source is placed the side are given in Fig. 6 around the source at chosen time points. The steady state solution in this case is given along with these for effective comparison. The one-dimensional plots of the transient temperature behavior at source location for this case is plotted in Fig. 7. The transient behavior is similar to the trend observed in cylindrical case (Fig. 5) except the time required for reaching the steady-state in this case is much larger.

E. Breast Tissue

The source in here was also modeled similar to brain case except beam radius was 0.5 mm and power as 17 mW. This case actually considers the worst case scenario in terms of using modern THz source [8]. The transient behavior of the temperature raise is given in Figs. 8 and 9. Similar to earlier case, the temperature raise that was observed in this case is much higher compared to brain tissue (Fig. 6 and 7), as the THz source power is higher and beam radius is smaller, but the transient behavior (trend) to reach the steady state is similar.

F. Effect of THz spot radius

As mentioned earlier, it is hard to focus the THz beam spot radius below 0.25 mm [14], which forms the worst case scenario. To effectively study the temperature raise as a function of spot radius, we have considered the breast tissue

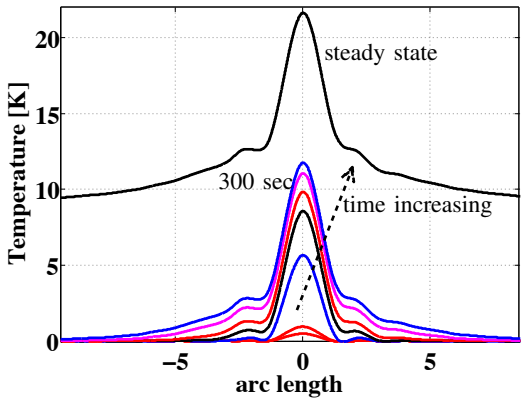

Fig. 8. An one-dimensional plot showing the time-dependent behavior of temperature raise around source (arc length = 0) in the breast model. The time points that were shown here correspond to 0.5, 1, 10, 30, 60, 150, and 300 sec along with steady-state solution. The input parameters for the model are given in Table-I with THz beam radius $a = 0.5$ mm with the power $P = 17$ mW.

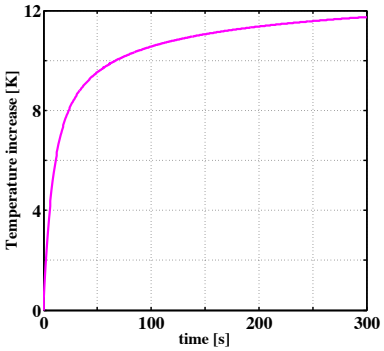

Fig. 9. The transient behavior of temperature raise at the source location corresponding to Fig. 8.

(as the nodal distance in this case was around 0.5 mm) with the power of THz source as 17 mW similar to earlier case. The spot radius was chosen to be 0.25 mm, 1 mm, 2.5 mm, and 5 mm and the observed temperature raise in the ROI is given in Fig. 10 at t = 60 sec and steady-state case. The beam spot radius being 0.5 mm result is already presented in the Fig. 8 (first and last column of the second row). The time point choice of 1 minute (top row of Fig. 10) indicates worst case exposure time for a typical THz biomedical application. The results indicate that the raise in the temperature could be as high as 39 ^{o}K for THz exposure of 1 minute using the modern sources for the worst case of beam spot radius being 0.25 mm. The beam spot radius of 2.5 mm could be considered as the most practical case, which shows the temperature raise of 1.5 ^{o}K.

IV. Discussion

Typical safety limits on the heating effects caused by electromagnetic radiation is expressed in terms of Specific Absorption Rate (SAR). The SAR in these studies is determined by the formulations used in hyperthermia areas [26] and is

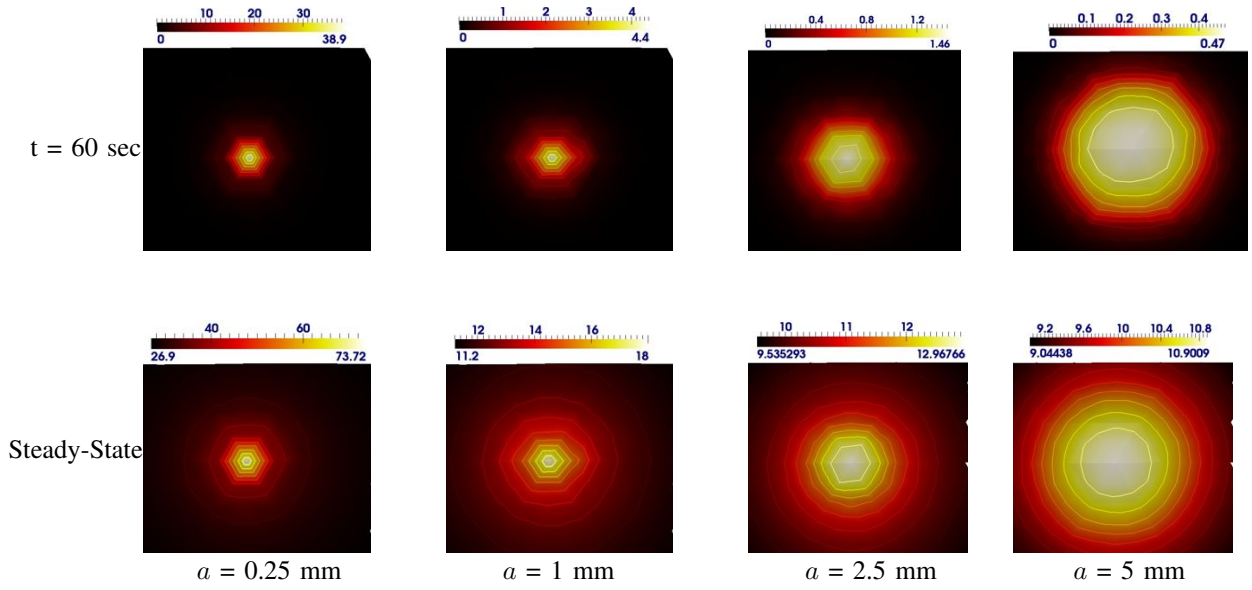

Fig. 10. THz beam spot radius (a) dependent behavior of temperature raise in the region of interest (12 mm X 12 mm centered around source, shown in Fig. 2) in case of breast model. The power of the THz source is assumed to be P = 17 mW. Top row shows the temperature raise for the exposure time being 60 seconds and the corresponding steady-state solution is given in the bottom row.

defined as [12]

$$\text{SAR} = \frac{c_p \triangle T}{\triangle t} \tag{6}$$

with $\triangle T$ indicating the increase in the temperature observed during time $\triangle t$. Also as specific heat (c_p) is a inherent property of tissue type, the SAR varies accordingly, leading to different safety limits based on the tissue type. Even though the determination of safety limits is beyond the scope of this work, but SAR values could be easily determined from the developed methodology. Determination of such SAR values are very critical in planning any experiments involving biological tissues. Methodologies that were developed here gives a tool for such computations. Also note that from Eq. 6, it is evident that SAR is directly proportional to temperature raise in a tissue type and the exposure levels correspond to raise in maximum temperatures, which is determined for the two cases discussed here.

Note that computations performed here represent the worst-case scenario, wherein the heat exchange mechanisms (convection and radiation) are excluded in the numerical model, which might be necessary in determining the exact value of highest thermal load. Such determination require both THz and thermal simulations. When the THz propagation problem is well defined in terms of geometry, radiating structure, power level, etc, and do not vary, the temperature raise could be calculated by considering only heat conduction [12].

The obtained steady state behavior using the same inputs as given in Ref. [15] from the FEM technique as observed in Fig. 3 in both radial and axial directions showed that the model that is applied in this work correlates very well with the earlier reported values. The discrepancy in the raise in temperature in the axial direction for the FEM case is primarily due to the coarser nature of mesh in this direction. This discrepancy could be reduced further, if a finer mesh is used with a caveat that the computational complexity in these cases will be much higher. Note that temperature profiles shown in this work has been limited to the ROI for better clarity/presentation as the raise in the temperature is highly localized.

In the FEM scheme, piecewise linear finite elements and backward Euler method are used for the spatial and temporal discretizations, respectively. These discretizations provide first order convergence in both space and time. In order to increase the spatial convergence rate and reduce the numerical error (spatial), higher order finite elements could be used. However, it will increase the computational cost. Alternatively, we could also use an adaptive finite element mesh to further reduce the numerical error. The main aim of the study is to compute the maximum raise in temperature in a given model, the convergence studies along with techniques that reduce the numerical error were not taken up in this work.

The numerical accuracy of the solutions presented in here highly depend on the mesh size (number of vertices) and THz beam spot radius. Cases where the nodal distance is greater than the beam spot diameter was shown to give erroneous results due to source modeling problems. Decreasing the nodal distance uniformly through out the mesh, in turn increasing the number of vertices, increase computational complexity and requires more powerful computational setup to achieve the desired accuracy. The better solution is to perform adaptive meshing, where less nodal distance is chosen in the heating zone resulting in fine mesh in ROI and more coarser mesh else where. Such choice can be achieved by means of convergence and sensitivity tests, which is beyond the scope of this work and will be taken up as a future extension to the presented work.

The temperature raise depicted in the realistic tissue case

that were considered here have been dealt with sources being place at only one location and assuming that only one source is illuminated at a time. In a THz tomography setup [27], it might be likely that more than one source might be active. As observed from the results here, the heat raise tends to be highly localized around the source point, making the modeling performed as in this work valid for the tomography equipment as well.

As pointed out in Ref. [15], the temperature raise observed through modeling is highly dependent on beam width. Even though it is not shown here, the temperature raise for a narrower beam is higher and becomes more localized compared to wider THz beams. For narrower beam radius, the temperature raise could be as higher as 39 ^oK with 1 minute exposure, asserting that this could permanently damage the tissue under investigation. Among the brain and breast cases, it is observed in here that the temperature raise in brain is comparatively higher (maximum temperature raise of 1.2^oK to 0.24^oK with the THz beam spot radius being 2 mm and power being 1 mW) due to the presence of CSF layer in the brain. This also asserts that the temperature effects of the THZ radiation is going to be non-uniform through out the body, in case where THz will be used *in-vivo* scenario.

The computation times associated with each of these models for a time step is less than a second with eight processors, as the linear system of equations that were solved at each time step is sparse, symmetric, and positive definite. The computational complexity could be further reduces with the deployment more processors. The memory usage in all these computations are dependent on the finite element mesh that is used, typically the band-width optimized ones providing better computational efficiency.

V. Conclusions

The THz applications are gaining momentum in both biological as well as defense areas, where the current emphasis is on making them as non-invasive procedures. The planning/setting up of experiments using the biological tissues should have consideration towards safety limits. The finite element based methodology here can provide the worst-case scenario estimations of temperature raise in tissue types, giving immense flexibility towards modeling irregular and inhomogeneous tissue types. The investigation here also revealed that the heating effects are not uniform for all tissues and mainly dependent on the constituents of tissues. The methodologies here assumed that THz radiation will be employed *in-vivo* scenarios, where the real-time measurements of temperature is not possible always and only models could be employed to estimate the temperature raise and provide SAR towards knowing the safety limits.

Acknowledgment

The authors are thankful to the anonymous reviewer for his/her comments, which greatly improved the content and presentation of this work. P.K.Y. acknowledges the Department of Atomic Energy, Government of India through DAE young scientist research award (Sanction No. 2010/20/34/6/BRNS).

References

[1] E. P. J. Parrott, Y. Sun, and E. Pickwell-MacPherson, "Terahertz spectroscopy: Its future role in medical diagnoses," Journal of Molecular Structure, 1006(1–3), 66-76 (2011).

[2] A. J. Fitzgerald, V. P. Wallace, M. Jimenez-Linan, L. Bobrow, R. J. Pye, A. D. Purushotham, and D. D. Arnone, "Terahertz pulsed imaging of human breast tumors," Radiology 239(2), 533–540 (2006).

[3] P. C. Ashworth, E. Pickwell-MacPherson, E. Provenzano, S. E. Pinder, A. D. Purushotham, M. Pepper, and V. P. Wallace, "Terahertz pulsed spectroscopy of freshly excised human breast cancer," Opt. Express 17, 12444–12454 (2009)

[4] E. Pickwell, A. J. Fitzgerald, B. E. Cole, P. F. Taday, R. J. Pye, T. Ha, M. Pepper, and V. P. Wallace, "Simulating the response of terahertz radiation to basal cell carcinoma using ex vivo spectroscopy measurements," J. Biomed. Opt. 10(6), 064021–064027 (2005).

[5] D. Crawley, C. Longbottom, V. P. Wallace, B. Cole, D. Arnone, and M. Pepper, "Three-dimensional terahertz pulse imaging of dental tissue," J. Biomed. Opt. 8(2), 303–307 (2003).

[6] D. Abbott and X. C. Zhang, "Scanning the issue: T-ray imaging, sensing, and detection," Proc. IEEE 95(8), 1509–1513 (2007).

[7] R. Appleby and H. B. Wallace, "Standoff detection of weapons and contraband in the 100 GHz to 1 THz region," IEEE Trans. Antennas Propag. 55, 2944–2956 (2007).

[8] C. Worral, J. Alton, M. Houghton, S. Barbieri, H. E. Beere, D. Ritchie andC. Sirtori, "Continuous wave operation of a superlattice quantum cascade laser emitting at 2 THz," Opt. Express 14, 171–181 (2006).

[9] Y.-S Lee, *Principles of Terahertz Science and Technology* (Springer, 2009).

[10] G. L. Carr, M. C. Martin, W. R. McKinney, K. Jordan, G. R. Neil and G. P. Williams, "High-power terahertz radiation from relativistic electrons," Nature 420, 153–156 (2002).

[11] M. Sherwin,"Terahertz power," Nature 420,131–132 (2002).

[12] T. Samaras, P. Regli, and N. Kuster. "Electromagnetic and heat transfer computations for non-ionizing radiation dosimetry," Phys. Med. Biol. 45, 2233–2246 (2000).

[13] A. G. Markelz, "Terahertz dielectric sensitivity to biomolecular structure and function," IEEE J. Sel. Top. Quantum Electron. 14(1), 180–190 (2008).

[14] E. Berry, G. C. Walker, A. J. Fitzgerald, N. N. Zinovev, M. Chamberlain, S. W. Smye, R. E. Miles, and M. A. Smith, "Do in vivo terahertz imaging systems comply with safety guidelines?" J. Laser Appl. 15, 192–198 (2003).

[15] T. T. L. Kristensen, W. Withayachumnankul, P. U. Jepsen, and D. Abbott, "Modeling terahertz heating effects on water," Opt. Express 18, 4727–4739 (2010).

[16] V. Thomee, *Galerkin Finite Element Methods for Parabolic Problems*, Second Edition, Springer, 2006.

[17] G. Karypis and V. Kumar, "A Fast and Highly Quality Multilevel Scheme for Partitioning Irregular Graphs," SIAM Journal on Scientific Computing 20(1), 359–392 (1999).

[18] P. R. Amestoy, I. S. Duff, J. Koster and J.-Y. L'Excellent, "A Fully Asynchronous Multifrontal Solver Using Distributed Dynamic Scheduling," SIAM J. Mat. Anal. Appl. **23**, 15–41 (2001).

[19] H. Si, "TetGen: A Quality Tetrahedral Mesh Generator and a 3D Delaunay Triangulator," Weblink: http://tetgen.berlios.de/ (accessed on: March 31, 2012).

[20] D. L. Collins, A. P. Zijdenbos, V. Kollokian, J. G. Sled, N. J. Kabani, C. J. Holmes, and A. C. Evans, "Design and construction of a realistic digital brain phantom," IEEE Trans. Med. Imaging 17(3), 463–468 (1998).

[21] Q. Fang, "Mesh-based Monte Carlo method using fast ray-tracing in Plucker coordinates," Biomed. Opt. Express 1(1), 165–175 (2010).

[22] C. M. Carpenter, S. Srinivasan, B. W. Pogue, and K. D. Paulsen, "Methodology development for three-dimensional MR-guided near infrared spectroscopy of breast tumors," Opt. Express **16**, 17903–17914 (2008).

[23] W. F. Cheong, S. A. Prahl, and A. J. Welsh, "A review of the optical properties of biological tissues," IEEE J. Quantum Electron. 26, 2166–2185 (1990).

[24] J. Xu, K. W. Plaxco and S. J. Allen, "Absorption spectra of liquid water and aqueous buffers between 0.3 and 3.72 THz," J. Chem. Phys. 124, 1–3 (2006).

[25] E. J. Berjano, "Theoretical modeling for radiofrequency ablation: state-of-the-art and challenges for the future," Biomed Eng Online 5, 24:1–17 (2006).

[26] R. B. Roeme, "Engineering Aspects of Hyperthermia Therapy," Annual Review of Biomedical Engineering 1, 347–376 (1999).
[27] S. Wang and X-C. Zhang, "Pulsed Terahertz Tomography," J. Phys. D: Appl. Phys. 37, R1–R36 (2004).

Sashikumaar Ganesan is an assistant professor in Supercomputer Education and Research Centre at Indian Institute of Science, Bangalore. He received Dr.rer.nat degree in Mathematics from Oto-von-Guericke University in 2006 and holds a M.Sc. degree in Mathematics from Bharathidasan University, Tiruchirappalli. His research interests include finite element analysis and parallel algorithms.

Phaneendra K. Yalavarthy received the M.Sc. degree in engineering from the Indian Institute of Science, Bangalore, India, in 2004, and the Ph.D. degree in biomedical computation from Dartmouth College, Hanover, NH, in 2007.

He is an Assistant Professor in the Supercomputer Education and Research Centre, Indian Institute of Science, Bangalore. His research interests include medical image computing, medical image analysis, and biomedical optics.